
MODELING THE MECHANOSENSITIVE COLLECTIVE MIGRATION OF CELLS ON THE SURFACE AND THE INTERIOR OF MORPHING SOFT TISSUES

A PREPRINT

Jaemin Kim

Sibley School of Mechanical and Aerospace Engineering
Cornell University
Ithaca, NY 14853, USA

Mahmut Selman Sakar

Institutes of Mechanical Engineering and Bioengineering
Ecole Polytechnique Fédérale de Lausanne
Lausanne, Switzerland

Nikolaos Bouklas*

Sibley School of Mechanical and Aerospace Engineering
Cornell University
Ithaca, NY 14853, USA

October 17, 2023

ABSTRACT

Cellular contractility, migration, and extracellular matrix (ECM) mechanics are critical for a wide range of biological processes including embryonic development, wound healing, tissue morphogenesis, and regeneration. Even though the distinct response of cells near the tissue periphery has been previously observed in cell-laden microtissues, including faster kinetics and more prominent cell-ECM interactions, there are currently no models that can fully combine coupled surface and bulk mechanics and kinetics to recapitulate the morphogenic response of these constructs. Mailand *et al.* (2019) had shown the importance of active elastocapillarity in cell-laden microtissues, but modeling the distinct mechanosensitive migration of cells on the periphery and the interior of highly deforming tissues has not been possible thus far, especially in the presence of active elastocapillary effects. This paper presents a framework for understanding the interplay between cellular contractility, migration, and ECM mechanics in dynamically morphing soft tissues accounting for distinct cellular responses in the bulk and the surface of tissues. The major novelty of this approach is that it enables modeling the distinct migratory and contractile response of cells residing on the tissue surface and the bulk, where concurrently the morphing soft tissues undergoes large deformations driven by cell contractility. Additionally, the proposed model is validated through simulation results that capture the changes in shape and cell concentration for wounded and intact microtissues, enabling the interpretation of experimental data. The numerical procedure that accounts for mechanosensitive stress generation, large deformations, diffusive migration in the bulk and a distinct mechanism for diffusive migration on deforming surfaces is inspired from recent work on bulk and surface poroelasticity of hydrogels involving elastocapillary effects, but in this work a two-field weak form is proposed and is able to alleviate numerical instabilities that were observed in the original method that utilized a three-field mixed finite element formulation.

*Corresponding author, nb589@cornell.edu

Keywords Morphogenesis · Mechanotransduction · Microtissue · Contractility · Cell migration · Wound healing

1 Introduction

The study of the physical interactions between cells and the surrounding extracellular matrix (ECM) is instrumental for diverse fields, including developmental biology, orthopedics, physiotherapy and oncology [Chen et al., 2007, Ma et al., 2008, Watt and Fujiwara, 2011]. The ability to manipulate and guide these interactions is crucial to engineer implantable tissues for regenerative medicine [Schmidt and Baier, 2000, Tepole, 2017]. The interactions between cells and ECM involve dynamic feedback loops that coordinate physiological responses to maintain an equilibrium state, which is called “homeostasis” [Brown et al., 1998, Humphrey, 2003, Eichinger et al., 2021a]. When the homeostatic state is disrupted, cells respond to restore the integrity, architecture, and function of the underlying tissue through a cascade of mechanical events that involve cell migration and matrix remodelling [Hinz et al., 2012, Nour et al., 2019, Cai et al., 2007].

Remodeling in connective tissues is driven by traction forces applied by fibroblasts residing inside and on the surface of the tissues [Grinnell and Petroll, 2010, Mammoto and Ingber, 2010, Foolen et al., 2015, Pereira et al., 2016, Van Helvert et al., 2018, Matis, 2020]. Reconstituted collagen and fibrin gels seeded with fibroblasts serve as “tissue equivalents” for the study of mechanical interactions among cells and the surrounding fibrous matrix [Bell et al., 1979, Stopak and Harris, 1982, Holle et al., 2016, Eichinger et al., 2021b,a]. Existing experimental platforms provide limited information on the distribution of stress and strain within the tissue equivalents. Given the complexity of the problem, advanced mathematical models that can interpret experimental data, isolate the factors influencing mechanical behavior at the cellular and tissue levels, and predict biomechanical responses in novel contexts are urgently needed [Humphrey, 2003, Eichinger et al., 2021b]. These mathematical models can also facilitate hypothesis-driven research [Kim et al., 2023a].

Tissue remodelling is a multi-scale process, and hence, various models have been developed to capture the behavior of cells with varying details, including molecular dynamics (MD) simulations, agent-based models, and continuum models with phenomenological interaction rules [Shaebani et al., 2020]. Although MD simulations and agent-based modeling offer a high degree of spatial resolution, they become impractical for studying large-scale tissue mechanics involving many cells [Wang and Xu, 2020]. To overcome this limitation, continuum approaches that model locally averaged details of the cell/ECM dynamics have been proposed [Byrne and Drasdo, 2009]. A number of continuum models have been developed to investigate how cellular contractility and mechanosensing affect tissue deformation. Certain models consider the effects of ECM alignment and dynamic cross-linking of ECM proteins [Legant et al., 2009, Deshpande et al., 2006, Vernerey and Farsad, 2011, Shenoy et al., 2016, Tepole, 2017, Ban et al., 2018, González-Valverde and García-Aznar, 2018, Baker et al., 2015, Abhilash et al., 2014] while other models captured the effects of cell migration [González-Valverde and García-Aznar, 2018, Banerjee and Marchetti, 2019, Kim et al., 2020, Mailand et al., 2021, Kim et al., 2023a]. None of these models have taken into account the distinct responses of cells residing on the surface and in the core of the fibrous tissue, despite growing experimental evidence suggesting a connection between cell migration and the geometric and mechanical properties of the tissue [Legant et al., 2012, Sunyer et al., 2016, Grolman et al., 2020]. Indeed, cells residing on the surface of a tissue experience a very different physical environment than the cells surrounded by a network of dense matrix.

In our previous work, we demonstrated that surface stresses arise in constrained fibroblast-populated collagen gels, leading to the morphogenesis of fibrous microtissues [Mailand et al., 2019]. We introduced computational models that incorporate both surface and bulk contractile stresses with the passive elasticity of the ECM in 2D [Mailand et al., 2019] and 3D [Kim et al., 2020]. More recently, we updated the model to account for the interplay between cell migration, contractility, and ECM mechanics in a dynamically morphing soft tissue [Kim et al., 2023a]. In that framework, cell migration occurs through a combination of active cell migration and passive tissue deformation. As cells generate contractile stresses, the tissue contracts and deforms. If the tissue is mechanically constrained, an inhomogeneous stress field could arise. Cells are modeled as mechanosensitive in a way that they actively move to regions where they can apply higher forces. An important limitation in [Kim et al., 2020], is that the surface cell concentration is directly tied to the bulk cell concentration, and cells cannot move in a different modality on the surface or in the bulk, and there can also be no exchange between the two species populations. To further advance our understanding of the interplay between cellular mechanics and tissue morphogenesis, it is instrumental to develop a continuum mechanics framework that accounts for distinct surface cell kinetics on deforming soft bodies.

The theoretical foundation of this formulation has been explored in few recent publications. McBride et al. [2011] presented a nonlinear theory to account for species migration in both the bulk and on surfaces but did not present a computational framework. Lucantonio et al. [2016] further specialized this theory for thermo-responsive hydrogels and membranes and applied it to drug delivery systems, and also presented a mixed finite element formulation for the problem. A more recent study by Kim et al. [2023b] has extended this framework for hydrogels in lengthscales where

surface effects (e.g. surface tension) could be important and drive deformation and species migration in the bulk and on the free surfaces of the materials, leading to complex concentration profiles at equilibrium; where a mixed finite element formulation was also presented. These advancements open up exciting possibilities for investigating complex biological systems, such as cell-ECM systems where collective migration and contraction of cells is distinct on the tissue periphery and in the bulk, and “active” surface effects become prominent.

Here, we present a continuum mechanics framework that can account for both surface and bulk cell migration and tissue contractility in dynamically morphing soft tissues, along with a corresponding finite element implementation in a total Lagrangian setting. The proposed model allows for cells to migrate in the bulk, on the deforming tissue surfaces, and also transition between the bulk and the surface while allowing for cell/ECM interactions. The model incorporates the coupling of cell concentration and local deformation state with both the associated contractile stress generation and cell migration. In Section 2, we summarize the proposed continuum theory. Section 3 propose the novel free energy for mechanosensitive cell migration and contractility. Section 4 presents the finite element formulation and Section 5 presents simulations of morphing microtissues and wound closure.

2 A nonlinear theory

We present a novel phenomenological continuum framework that accounts for the distinct response of mesenchymal cells contracting and migrating in extracellular matrix (ECM) to recapitulate tissue-level mechanics. Our theory accounts the temporal coupling between cell migration and contractility, resulting in an equilibrium homeostatic state that describes inhomogeneous 3D deformation and cell concentration. In our notation, $\{\bullet\}$ and $\{\tilde{\bullet}\}$ denote bulk and surface quantities, respectively, for a body occupying a volume V bounded by an outer surface denoted as S . It is important to note that a surface quantity is not equivalent to the bulk quantity evaluated on the surface. The general notation convention and nomenclature follow [Kim et al., 2023b], where the reader can also follow some of the key concepts in differential geometry necessary for the description of the kinematics of deforming surfaces.

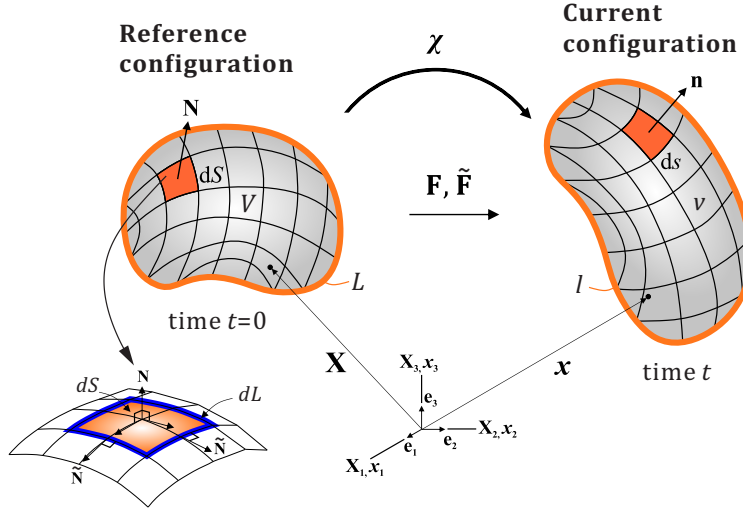


Figure 1: Schematic illustration of the reference and current state of a continuum body. The reference volume and surface, and boundary are denoted by V and S , and L respectively. The normal vector to the surface in the reference and current configuration (\mathbf{N} and \mathbf{n}) and the bi-normal vector to the boundary ($\tilde{\mathbf{N}}$) are shown, where the over-tilde indicates surface quantities.

2.1 Kinematics

Let V be a fixed reference configuration of a continuum body \mathcal{B} . We use the notation $\chi : V \rightarrow \mathbb{R}^3$ for the deformation of body \mathcal{B} . A motion χ is the vector field of the mapping $\mathbf{x} = \chi(\mathbf{X})$, of a material point in the reference configuration $\mathbf{X} \in V$ to a position in the deformed configuration $\mathbf{x} \in v$. The kinematics of a typical particle are described by the displacement vector field in the spatial description, $\mathbf{u}(\mathbf{X}, t) = \mathbf{x}(\mathbf{X}, t) - \mathbf{X}$. The kinematics of an infinitesimal bulk

element are described by

$$\mathbf{F}(\mathbf{X}, t) = \frac{\partial \chi(\mathbf{X}, t)}{\partial \mathbf{X}} = \nabla_{\mathbf{X}} \mathbf{x}(\mathbf{X}, t) \quad (1a)$$

$$\mathbf{F}^{-1}(\mathbf{x}, t) = \frac{\partial \chi^{-1}(\mathbf{x}, t)}{\partial \mathbf{x}} = \nabla_{\mathbf{x}} \mathbf{X}(\mathbf{x}, t) \quad (1b)$$

where $\mathbf{F}(\mathbf{X}, t)$ and $\mathbf{F}^{-1}(\mathbf{x}, t)$ are the deformation gradient and inverse deformation gradient, respectively. Note that $J(\mathbf{X}, t) = dv/dV = \det \mathbf{F}(\mathbf{X}, t) > 0$ is the Jacobian determinant defining the ratio of a volume element between the material and spatial configuration.

The surface displacement $\tilde{\mathbf{u}}(\tilde{\mathbf{X}}, t)$ can be determined by $\mathbf{u}(\mathbf{X}, t)|_S = \tilde{\mathbf{u}}(\tilde{\mathbf{X}}, t)$, which imposes kinematic conformity between the bulk and the surface. The motion of an arbitrary differential vector element connecting two material points in the bulk can be mapped by the deformation gradient \mathbf{F} through the motion of the body. However, a unit normal vector \mathbf{N} in the material configuration cannot be transformed into a unit normal vector \mathbf{n} in the spatial configuration via the deformation gradient, as shown in Figure 1 [Holzapfel, 2000, Steinmann, 2008]. This motivates us to follow the kinematics of an infinitesimal surface element [Steinmann, 2008, Kim et al., 2020].

$$\tilde{\mathbf{F}}(\tilde{\mathbf{X}}, t) = \frac{\partial \chi(\tilde{\mathbf{X}}, t)}{\partial \tilde{\mathbf{X}}} \cdot \tilde{\mathbf{I}} = \tilde{\nabla}_{\tilde{\mathbf{x}}} \tilde{\mathbf{x}}(\tilde{\mathbf{X}}, t) \quad (2a)$$

$$\tilde{\mathbf{F}}^{-1}(\tilde{\mathbf{x}}, t) = \frac{\partial \chi^{-1}(\tilde{\mathbf{x}}, t)}{\partial \tilde{\mathbf{x}}} \cdot \tilde{\mathbf{i}} = \tilde{\nabla}_{\tilde{\mathbf{x}}} \tilde{\mathbf{X}}(\tilde{\mathbf{x}}, t) \quad (2b)$$

where $\tilde{\mathbf{F}}(\tilde{\mathbf{X}}, t)$ and $\tilde{\mathbf{F}}^{-1}(\tilde{\mathbf{x}}, t)$ are the surface deformation gradient and inverse surface deformation gradient. The $\tilde{\mathbf{I}} = \mathbf{I} - \mathbf{N} \otimes \mathbf{N}$ and $\tilde{\mathbf{i}} = \mathbf{i} - \mathbf{n} \otimes \mathbf{n}$ are the mixed surface unit tensors with the outward unit normal vectors \mathbf{N} and \mathbf{n} , where $\tilde{\mathbf{I}}$ and $\tilde{\mathbf{i}}$ act as a surface (idempotent) projection tensors in material and spatial configurations, respectively. Note that $\tilde{J}(\tilde{\mathbf{X}}, t) = da/dA = \det \tilde{\mathbf{F}}(\tilde{\mathbf{X}}, t) > 0$ is the surface Jacobian determinant defining the ratio of a surface element between material and spatial configuration.

The divergence theorems for bulk and surface are defined by [Green and Zerna, 1992, Steinmann, 2008]

$$\int_V \nabla_{\mathbf{x}} \cdot \{\bullet\} dV = \int_S \{\bullet\} \cdot \mathbf{N} dS \quad (3a)$$

$$\int_S \tilde{\nabla}_{\tilde{\mathbf{x}}} \cdot \{\tilde{\bullet}\} dS = \int_L \{\tilde{\bullet}\} \cdot \tilde{\mathbf{N}} dL - \int_S \tilde{\kappa} \{\tilde{\bullet}\} \cdot \mathbf{N} dS \quad (3b)$$

where $\tilde{\mathbf{N}}$ is the unit outward bi-normal vectors to the boundary curve, L , and $\tilde{\kappa} = -\tilde{\nabla}_{\tilde{\mathbf{x}}} \cdot \mathbf{N}$ is total curvature (twice the mean surface curvature).

We decompose the deformation gradient into a volumetric and an isochoric part, $\mathbf{F} = (J^{1/3} \mathbf{I}) \bar{\mathbf{F}}$, where $J^{1/3} \mathbf{I}$ and $\bar{\mathbf{F}}$ are associated with volumetric and isochoric deformation. Following, we utilize $\{\bullet\}$ to denote quantities associated with the isochoric part of the deformation gradient. We introduce the strain measures as follows:

$$\mathbf{C} = \mathbf{F}^T \mathbf{F} \quad \text{and} \quad I_1 = \text{tr}(\mathbf{C}) \quad (4a)$$

$$\bar{\mathbf{C}} = \bar{\mathbf{F}}^T \bar{\mathbf{F}} \quad \text{and} \quad \bar{I}_1 = \text{tr}(\bar{\mathbf{C}}) \quad (4b)$$

where \mathbf{C} and I_1 are the right Cauchy-Green tensor and its first principal invariant, and $\bar{\mathbf{C}}$ and \bar{I}_1 are the modified right Cauchy-Green tensor and its first principal invariant.

We introduce the right Cauchy-Green tensors on the surface as

$$\tilde{\mathbf{C}} = \tilde{\mathbf{F}}^T \tilde{\mathbf{F}} \quad (5)$$

Note that we cannot directly obtain the inverse of the surface right Cauchy-Green tensor due to the fact that it is not full rank (a characteristic that it inherits from the surface deformation gradient tensor). Nevertheless, we can still obtain its inverse form in the generalized sense,

$$\tilde{\mathbf{C}}^{-1} = \tilde{\mathbf{I}} \mathbf{C}^{-1} \tilde{\mathbf{I}} \quad (6)$$

which will be utilized in the forthcoming developments for defining the surface kinetic law. The detailed derivation for the surface kinematics can be found in Green and Zerna [1992], Steinmann [2008], Do Carmo [2016].

2.2 Equilibrium

Mechanical equilibrium is assumed to be maintained at all time during the transient process neglecting inertial terms and body forces.

$$\nabla_{\mathbf{x}} \cdot \mathbf{P} + \mathbf{B} = 0 \quad \text{in } V \quad (7a)$$

$$\mathbf{P}\mathbf{N} - \tilde{\nabla}_{\tilde{\mathbf{x}}} \cdot \tilde{\mathbf{P}} = \mathbf{T} \quad \text{on } S_T \quad (7b)$$

$$\mathbf{u} = \mathbf{u}_p \quad \text{on } S_u \quad (7c)$$

$$[[\tilde{\mathbf{P}}\tilde{\mathbf{N}}]] = 0 \quad \text{on } L \quad (7d)$$

where \mathbf{P} and $\tilde{\mathbf{P}}$ are the first Piola-Kirchoff (PK1) stress in bulk and on surface, \mathbf{B} and \mathbf{T} are the body force and the traction vector, \mathbf{u} is the displacement, and \mathbf{u}_p is the prescribed displacement on the Dirichlet part of the boundary condition. Note that a Neumann-type boundary condition is also defined on boundary curves that $[[\bullet]]$ indicates summation over surfaces intersecting on boundary curves [Steinmann, 2008].

2.3 Cell balance law

Through species balance, the equations for the rate of change of nominal cell concentration, \dot{C} and $\dot{\tilde{C}}$ are obtained [McBride et al., 2011]:

$$\dot{C} + \nabla_{\mathbf{x}} \cdot \mathbf{J} = r \quad \text{in } V \quad (8a)$$

$$\dot{\tilde{C}} + \tilde{\nabla}_{\tilde{\mathbf{x}}} \cdot \tilde{\mathbf{J}} - \mathbf{J} \cdot \mathbf{N} = i \quad \text{on } S_{\tilde{C}} \quad (8b)$$

$$\tilde{\mathbf{J}} = \tilde{\mathbf{J}}_p \quad \text{on } S_{\tilde{\mathbf{J}}} \quad (8c)$$

$$[[\tilde{\mathbf{J}} \cdot \tilde{\mathbf{N}}]] = 0 \quad \text{on } L \quad (8d)$$

where \dot{C} and $\dot{\tilde{C}}$ are the rate of change of nominal species concentration in the bulk and on the surface, \mathbf{J} and $\tilde{\mathbf{J}}$ indicate the nominal flux of species in the reference configuration. The r and i are the source/sink terms for the number of cells injected into the reference volume and area per unit time, which can be attributed to proliferation/apoptosis. $\tilde{\mathbf{J}}_p$ is the prescribed surface flux. The Equation (8) are supplemented with initial and boundary conditions

$$C = C_0 \quad \text{at } t = 0 \quad (9a)$$

$$\tilde{C} = \tilde{C}_0 \quad \text{at } t = 0 \quad (9b)$$

where C_0 and \tilde{C}_0 are the initial nominal species concentration at time $t = 0$. It is important to note that we neglect cell proliferation/apoptosis in the bulk $r = 0$ and on the surface $i = 0$ for this work, which could be very important as we study other systems.

2.4 Constitutive relations

It has been observed that cells located near the tissue boundary exhibit significantly more polarization than those in the bulk [Mailand et al., 2019, Kim et al., 2020]. Hence, besides the free energy density in the bulk, the free energy density on the surface must also be taken into account. We will use the terms ‘‘bulk’’ and ‘‘surface’’ to denote the respective free energy densities.

$$\Psi(\mathbf{F}, C, \eta) \quad \text{and} \quad \tilde{\Psi}(\tilde{\mathbf{F}}, \tilde{C}, \tilde{\eta}) \quad (10)$$

Following from Appendix A, the parentheses of the first six terms in Equation (33) must be zero to satisfy the inequality for any arbitrary $\dot{\mathbf{F}}$, $\dot{\tilde{\mathbf{F}}}$, \dot{C} and $\dot{\tilde{C}}$, which results in the constitutive relations as follows:

$$\mathbf{P} = \frac{\partial \Psi}{\partial \mathbf{F}}, \quad \mu = \frac{\partial \Psi}{\partial C}, \quad \xi = \frac{\partial \Psi}{\partial \eta} \quad (11a)$$

$$\tilde{\mathbf{P}} = \frac{\partial \tilde{\Psi}}{\partial \tilde{\mathbf{F}}}, \quad \tilde{\mu} = \frac{\partial \tilde{\Psi}}{\partial \tilde{C}}, \quad \tilde{\xi} = \frac{\partial \tilde{\Psi}}{\partial \tilde{\eta}} \quad (11b)$$

where \mathbf{P} and $\tilde{\mathbf{P}}$ represent the first Piola-Kirchhoff (PK) stress tensors in the bulk and on the surface, respectively. The variables μ and $\tilde{\mu}$ denote the bio-chemical potential in the bulk and on the surface, respectively. The microscopic forces generated by cells and applied to the ECM network are represented by ξ in the bulk and $\tilde{\xi}$ on the surface. It is important

to note that the microscopic forces indicate that an increase in the activation level results in an increase in the force exerted on the ECM network.

For the seventh term in Equation (33), the most obvious way to guarantee the dissipation inequality on surface is to impose the condition [McBride et al., 2011],

$$\mu(\mathbf{X}, t) = \tilde{\mu}(\tilde{\mathbf{X}}, t) \quad \text{on } S \quad (12)$$

which is the conformity of the bio-chemical potential between the surface and bulk.

The eighth and ninth terms in Equation (33) remain negative, respectively, and we adopt a kinetic law [Gurtin et al., 2010] to describe the consistent species diffusion that is driven by the bio-chemical potential. The kinetic law is given by:

$$\mathbf{J} = -\mathbf{M}\nabla_{\mathbf{x}}\mu \quad \text{with} \quad \mathbf{M} = CDC^{-1} \quad (13a)$$

$$\tilde{\mathbf{J}} = -\tilde{\mathbf{M}}\nabla_{\tilde{\mathbf{x}}}\tilde{\mu} \quad \text{with} \quad \tilde{\mathbf{M}} = \tilde{C}\tilde{D}\tilde{C}^{-1} \quad (13b)$$

Here, \mathbf{M} and $\tilde{\mathbf{M}}$ are positive-semidefinite mobility tensors in the bulk and on the surface, respectively. The effective diffusivity of the cells D in the bulk and \tilde{D} on the surface are assumed to be isotropic and independent of deformation and concentration as the simplest approximation [Bouklas and Huang, 2012]. The kinetic law describes the consistent migration of cells driven by the bio-chemical potential μ . Note that Fick's law for diffusion in the current configuration with a mobility constant M is pulled back to the reference configuration to derive our model.

3 Specific considerations for cell-laden microtissues

In this work, we will focus on a coupled framework for cell-ECM interaction of cell-laden contractile microtissues that considers bulk and surface "active" mechanics and kinetics. We have to specialize our choices for the surface and bulk free energy densities, corresponding constitutive laws, and definition of mobility tensors for our theory to be complete and to be able to proceed to the development of the numerical solution scheme.

3.1 A specific free energy

The free energy in the bulk should account for both passive and active contributions. The passive term captures the elasticity of the collagen network, which is typically considered nearly incompressible [Kim et al., 2020]. However, we allow for compressibility to accommodate tissue-level compaction generated by cell contractility. The active term captures the contractile action of fibroblasts residing in the bulk. On the other hand, the free energy on the surface only considers the active contribution, which captures the contractile action of fibroblasts on the surface and leads to a fluid-like response.

$$\Psi(\mathbf{F}, C) = \Psi_p(\mathbf{F}) + \Psi_a(\mathbf{F}, C) \quad \text{and} \quad \tilde{\Psi}_a(\tilde{\mathbf{F}}, \tilde{C}) \quad (14)$$

where the free energy density on the surface, $\tilde{\Psi}$, only considers the active contribution capturing the contractile action of fibroblasts on the surface, while the bulk free energy density Ψ is decomposed into the passive component Ψ_p due to elastic deformations of the ECM and the active component Ψ_a due to cell migration and contraction in the bulk. The active contribution on the surface is captured by $\tilde{\Psi}_a$, which takes into account the distinct mechanism of cell migration and contraction on the surface.

For the ECM response, we adopt a compressible neo-Hookean model [Holzapfel, 2000],

$$\Psi_p(\mathbf{F}) = \frac{G}{2} (\bar{I}_1 - 3) + \frac{K}{2} (J - 1)^2 \quad (15)$$

where G and K are the shear and bulk moduli, which can be uniquely defined by the Young's modulus E and Poisson's ratio ν . In order to capture the mechano-sensitive coupling that drives the competition of cell migration and contractility, we need to take into account the cell concentration and the level of activation of cell contraction, as well as the deformation. To this end, we propose a set of active free energy functions for the bulk and surface, which aim to capture the distinct mechanisms of cell migration and contraction.

$$\Psi_a(\mathbf{F}, C) = \frac{CJ}{C_0} \eta_\alpha + \frac{\beta}{2} \left(\frac{C}{C_0} - 1 \right)^2 \quad (16a)$$

$$\tilde{\Psi}_a(\tilde{\mathbf{F}}, \tilde{C}) = \frac{\tilde{C}\tilde{J}}{\tilde{C}_0} \eta_{\tilde{\alpha}} + \frac{\tilde{\beta}}{2} \left(\frac{\tilde{C}}{\tilde{C}_0} - 1 \right)^2 \quad (16b)$$

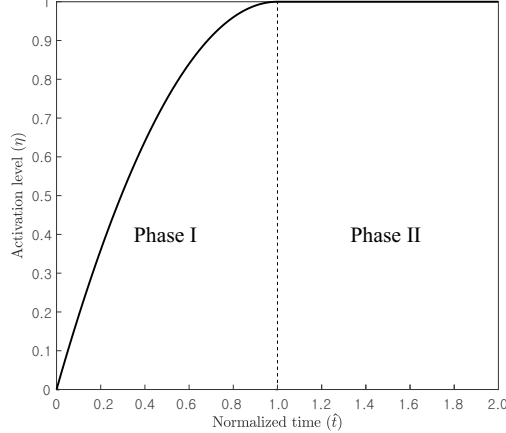


Figure 2: Activation level can map to two characteristic phases, a rapid increase (phase I) followed by a near-homeostatic state (phase II).

The first terms in Equations (16a) and (16b) represent the contribution of cell contractility and concentration to the free energy. Consistent with their definition in our previous work [Kim et al., 2023a], the terms $\eta_\alpha = \alpha\eta(t)$ and $\eta_{\tilde{\alpha}} = \tilde{\alpha}\eta(t)$ correspond to the bulk and surface contractile moduli, respectively, where α and $\tilde{\alpha}$ are the maximum allowable values modulated by the activation level $\eta(t)$. The activation level of the cell contractility can be viewed as a variable that reflects the stabilization of focal adhesions and stress fibers in the cell cytoskeleton [Humphrey et al., 2014, Eichinger et al., 2021a], that will be defined in Section 3.2. Note that CJ and $\tilde{C}\tilde{J}$ are the cell concentrations in the spatial configuration, which are normalized by the initial cell concentrations C_0 and \tilde{C}_0 . The second terms in Equations (16a) and (16b) regulate the cell distribution using a penalty approach, where β and $\tilde{\beta}$ are the penalty coefficients, and C/C_0 and \tilde{C}/\tilde{C}_0 are the ratios of cell concentration in the material configuration.

3.2 Activation level

Cells in living tissues interact with the extracellular matrix (ECM) to maintain homeostasis [Brown et al., 1998, Petroll et al., 2004, Paszek et al., 2005, Doyle et al., 2009, Eichinger et al., 2021a]. To capture the formation of stable focal adhesions between the cells and the ECM, and stable intracellular stress fibers, we have previously introduced a non-dimensional activation level of cell contractility, $\eta(t)$ [Kim et al., 2023a], that follows an equilibration process (see Figure 2). Living soft tissues exhibit two characteristic stages towards this equilibration process: (phase I) the contractile force increases rapidly, and (phase II) the force reaches a steady-state [Delvoye et al., 1991, Eastwood et al., 1996, Brown et al., 1998, Eichinger et al., 2020]. Given the complexity of tracking single cell forces, we suggest the following expression that approximately describes the dynamics of activation for all cells in the microtissue,

$$\eta(t) = \begin{cases} 1 - \left(1 - \frac{t}{\tau}\right)^n & (t \leq \tau) \\ 1 & (t > \tau) \end{cases} \quad (17)$$

In addition, we make the assumption, based on the conformity assumption in Equation Equation (12), that the activation level $\eta(t)$ is equal to the surface activation level $\tilde{\eta}(t)$ throughout the system. This assumption implies that the activation level is uniform and consistent across the bulk and surface regions.

$$\tilde{\eta}(t) = \eta(t) \quad (18)$$

In this context, the activation level $\eta(t)$ is a non-dimensional quantity that tracks the temporal stability of focal adhesions and the cells' ability to exert traction forces, with a range limited to $\eta(t) \in [0, 1]$. It should be noted that t represents the time elapsed since cell seeding, τ is the characteristic time for reaching equilibrium, and n is a dimensionless parameter. The reference configuration coincides with an initial unreformed state at zero activation level $\eta(t=0) = 0$, and the rise of $\eta(t > 0)$ triggers cell contractility and migration that ultimately lead to an equilibrium state. For this work, we assume a quadratic dependence ($n = 2$) for both active moduli (η_α and $\eta_{\tilde{\alpha}}$). Although it is exceedingly complex to track single cell forces, we suggest an approximate expression for the activation dynamics that is applicable to all cells in the microtissue.

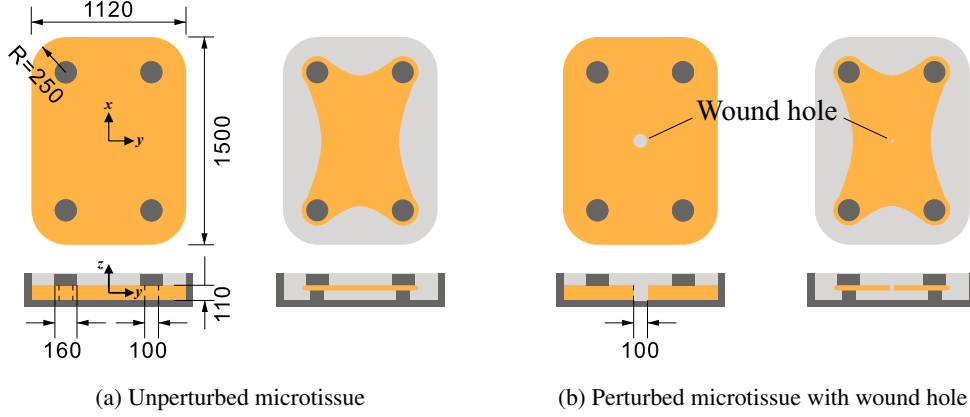


Figure 3: A schematic drawing for (a) an unperturbed microtissue and (b) and a microtissue with a cylindrical wound hole (unit: μm). The initial/undeformed (left) and final/equilibrium configurations (right) of microtissues are shown. The sectional view (bottom) is captured at the centerline of the top view (top).

3.3 Specific constitutive relations

The expression for the first PK stress tensors as well as the cell concentrations are calculated from Equation (11) using the free energy in Equations (14) to (16),

$$\xi = \frac{C}{C_0} \eta_\alpha J \quad (19a)$$

$$\tilde{\xi} = \frac{\tilde{C}}{\tilde{C}_0} \eta_{\tilde{\alpha}} \tilde{J} \quad (19b)$$

$$\mathbf{P} = GJ^{-2/3} \left(\mathbf{F} - \frac{1}{3} I_1 \mathbf{F}^{-T} \right) + K(J-1) J \mathbf{F}^{-T} + \xi \mathbf{F}^{-T} \quad (19c)$$

$$\tilde{\mathbf{P}} = \tilde{\xi} \tilde{\mathbf{F}}^{-T} \quad (19d)$$

$$\mu = \frac{\beta}{C_0} \left(\frac{C}{C_0} - 1 \right) + \frac{1}{C_0} \eta_\alpha J \Rightarrow C = \frac{C_0}{\beta} (C_0 \mu + \beta - \eta_\alpha J) \quad (19e)$$

$$\tilde{\mu} = \frac{\tilde{\beta}}{\tilde{C}_0} \left(\frac{\tilde{C}}{\tilde{C}_0} - 1 \right) + \frac{1}{\tilde{C}_0} \eta_{\tilde{\alpha}} \tilde{J} \Rightarrow \tilde{C} = \frac{\tilde{C}_0}{\tilde{\beta}} \left(\tilde{C}_0 \tilde{\mu} + \tilde{\beta} - \eta_{\tilde{\alpha}} \tilde{J} \right) \quad (19f)$$

where ξ and $\tilde{\xi}$ in Equations (19a) and (19b) are microscopic variables as the energy conjugate of the rate of activation level η , which allows us to capture the accurate representation of the system's behavior. As η evolves with time independently of deformation or chemical potential, ξ and $\tilde{\xi}$ are non-standard variables and are not used in the weak form for finite element implementation. Incorporating the coupled response allows us to capture the sensitivity of the contractile response to both cell concentration and collagen density [Eichinger et al., 2020] as well as the development of forces towards mechanical homeostasis [Brown et al., 1998]. It is important to note that while the activation level $\eta(t)$ evolves uniformly for all cells, the stresses that develop in the microtissue depend on the coupling of the activation level, the concentration of cells due to migration, and the deformation state. This can lead to an inhomogeneous stress state within the microtissue.

4 Mixed finite element formulation

This section presents a finite element formulation based on the nonlinear theory described in Sections 2 and 3. We start with the strong form of the governing equations and initial and boundary conditions. We then introduce the weak form of the problem and subsequently describe the temporal and spatial discretization and solution scheme. As the main focus of this research is the coupled mechanics between cell migration and tissue deformation in bulk and on surface, we neglect the terms associated with proliferation and apoptosis in the bulk and on the surface, i.e., $r = i = 0$, as a simplification.

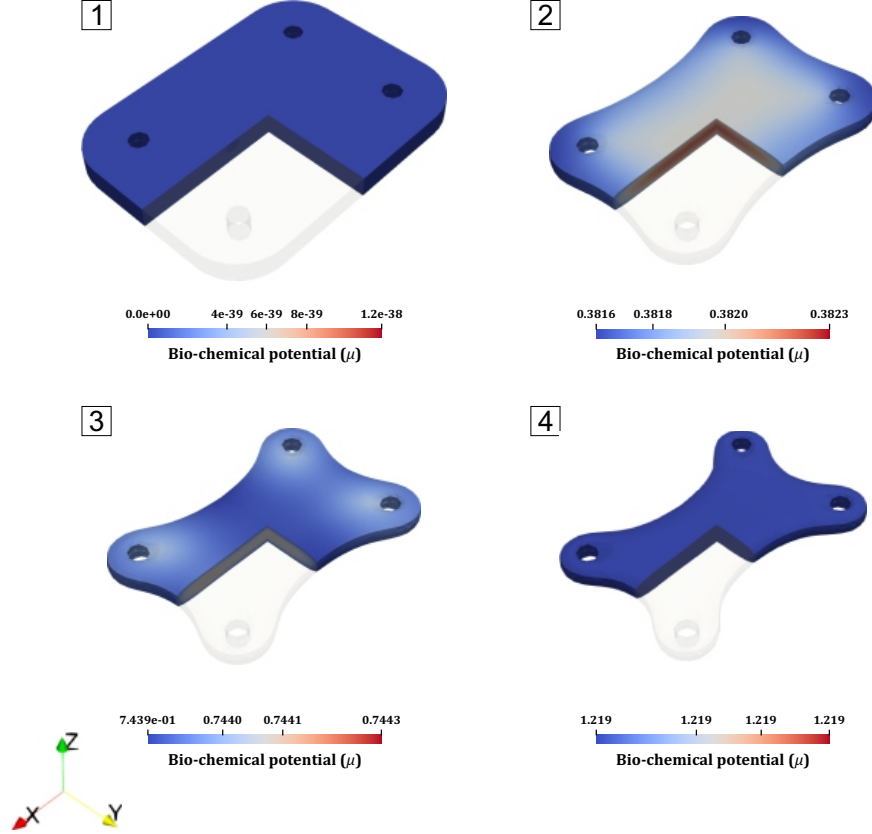


Figure 4: Temporal sequence of the bio-chemical potential during the formation of unperturbed microtissues. A quarter of the domain is made transparent to show the contour plot on two sections of the interior.

4.1 Two-field weak form

To simplify the finite element formulation and avoid the need for C^1 continuity requirements [Bouklas et al., 2015], we use the bio-chemical potential as the independent variable instead of cell concentration. The free energy densities are then expressed as a function of the deformation gradient and bio-chemical potential using a Legendre transform [Hong et al., 2008, McBride et al., 2011, Bouklas et al., 2015], which replaces a variable with its thermodynamic conjugate.

$$\Phi(\mathbf{F}, \mu, \eta) = \Psi(\mathbf{F}, C, \eta) - \mu C \quad (20a)$$

$$\tilde{\Phi}(\tilde{\mathbf{F}}, \tilde{\mu}, \tilde{\eta}) = \tilde{\Psi}(\tilde{\mathbf{F}}, \tilde{C}, \tilde{\eta}) - \tilde{\mu}\tilde{C} \quad (20b)$$

The weak form of the problem is obtained by using a set of test functions, which satisfy the necessary integrability conditions. By multiplying Equations (7a) and (8a) with $\delta \mathbf{u}$ and $\delta \mu$, and integrating over the domain, respectively, we obtain:

$$\int_V \mathbf{P} : \nabla_{\mathbf{X}} \delta \mathbf{u} \, dV + \int_S \tilde{\mathbf{P}} : \tilde{\nabla}_{\tilde{\mathbf{X}}} \delta \mathbf{u} \, dS = 0 \quad (21)$$

$$\int_V \dot{C} \delta \mu \, dV - \int_V \mathbf{J} \cdot \nabla_{\mathbf{X}} \delta \mu \, dV + \int_S \dot{\tilde{C}} \delta \mu \, dS - \int_S \tilde{\mathbf{J}} \cdot \tilde{\nabla}_{\tilde{\mathbf{X}}} \delta \mu \, dS = 0 \quad (22)$$

The weak form is a reformulation of the governing equations and boundary conditions that seeks to find trial functions for the displacement field $\mathbf{u}(\mathbf{X}, t)$ and bio-chemical potential $\mu(\mathbf{X}, t)$ that satisfy the equations, when tested against a set of permissible test functions $\delta \mathbf{u}$ and $\delta \mu(\mathbf{X})$. In our previous work [Kim et al., 2023b] on surface and bulk poroelasticity of hydrogels, we were not able to obtain a closed-form solution for the constitutive law governing the surface concentration. This led us to use a three-field weak form, which required solving an additional nonlinear equation for surface concentration in a weak sense, which led to oscillations near sharp features of the domain. Additionally, we have to note that the three-field weak form inherently has a saddle point structure. In this current work, we choose the specific free-energy formulation that enables us to obtain a two-field weak form without the need to solve an additional nonlinear equation, thereby avoiding numerical oscillations.

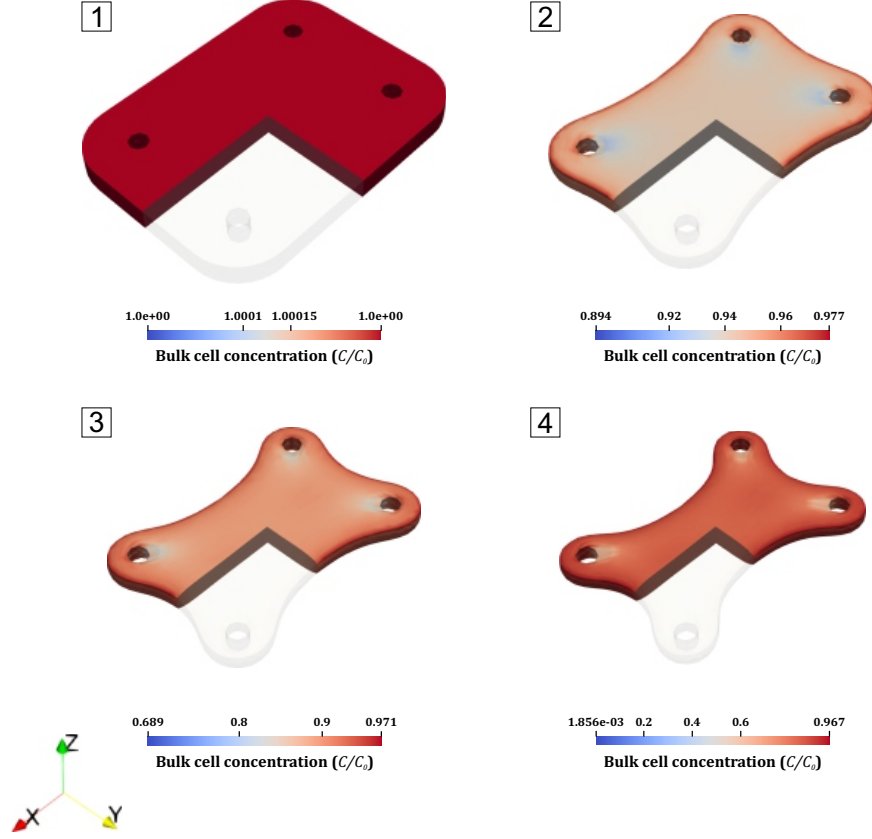


Figure 5: Temporal sequence of the bulk cell concentration during the formation of unperturbed microtissues. A quarter of the domain is made transparent to show the contour plot on two sections of the interior.

4.2 Temporal discretization

The backward Euler scheme is used to integrate Equation (22) over time:

$$\begin{aligned} & \int_V \frac{1}{\Delta t} (C^{t+\Delta t} - C^t) \delta\mu dV - \int_V \mathbf{J}^{t+\Delta t} \cdot \nabla_{\mathbf{X}} \delta\mu dV \\ & + \int_S \frac{1}{\Delta t} (\tilde{C}^{t+\Delta t} - \tilde{C}^t) \delta\mu dS - \int_S \tilde{\mathbf{J}}^{t+\Delta t} \cdot \tilde{\nabla}_{\tilde{\mathbf{X}}} \delta\mu dS = 0 \end{aligned} \quad (23)$$

where the superscripts indicate the time step, at the current time step $(t + \Delta t)$ or the previous step t . We can combine Equation (21) and Equation (23) as

$$\begin{aligned} & \int_V \mathbf{P} : \nabla_{\mathbf{X}} \delta\mathbf{u} dV + \int_V (C - C^t) \delta\mu dV - \Delta t \int_V \mathbf{J} \cdot \nabla_{\mathbf{X}} \delta\mu dV \\ & + \int_S \tilde{\mathbf{P}} : \tilde{\nabla}_{\tilde{\mathbf{X}}} \delta\mathbf{u} dS + \int_S (\tilde{C} - \tilde{C}^t) \delta\mu dS - \Delta t \int_S \tilde{\mathbf{J}} \cdot \tilde{\nabla}_{\tilde{\mathbf{X}}} \delta\mu dS = 0 \end{aligned} \quad (24)$$

where the superscript $(t + \Delta t)$ is omitted for all the terms at the current time step and C^t and \tilde{C}^t are the species concentration at the previous time step in the bulk and on the surface.

4.3 Spatial discretization

To solve for the displacement and bio-chemical potential fields simultaneously, a mixed finite element method is utilized. However, the mixed method can be numerically unstable if proper spatial discretization techniques are not employed [Bouklas et al., 2015]. To ensure numerical stability, an equal-order interpolation for displacement and bio-chemical potential was first tested, but it led to spurious oscillations in the solution. To overcome this issue, the MINI element [Arnold et al., 1984] was implemented, which uses equal-order interpolations for displacement and bio-chemical

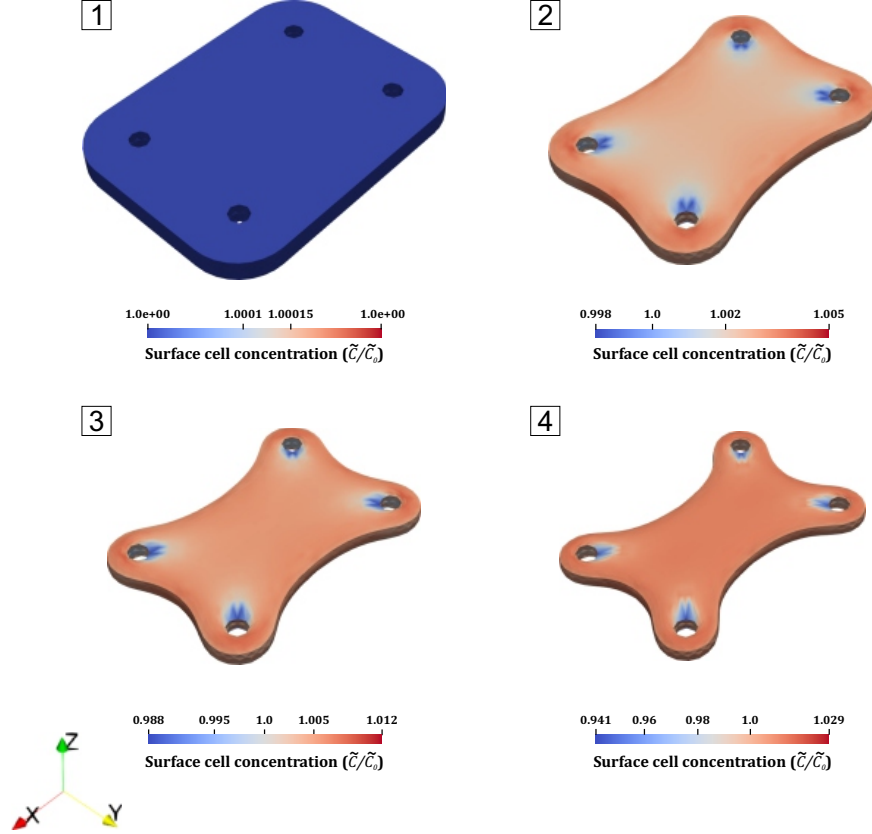


Figure 6: Temporal sequence of the surface cell concentration during the formation of unperturbed microtissues.

potential but enriches the interpolation for displacement with a bubble function [Boffi et al., 2013]. The displacement and bio-chemical potential are then interpolated throughout the domain of interest using the MINI element.

$$\mathbf{u} = \mathbf{H}^u \mathbf{u}^n \quad \text{and} \quad \mu = \mathbf{H}^\mu \boldsymbol{\mu}^n \quad (25)$$

where \mathbf{H}^u and \mathbf{H}^μ are the shape functions, \mathbf{u}^n and $\boldsymbol{\mu}^n$ are the nodal values of the displacement and bio-chemical potential, respectively. The test functions are discretized in the same way

$$\delta \mathbf{u} = \mathbf{H}^u \delta \mathbf{u}^n \quad \text{and} \quad \delta \mu = \mathbf{H}^\mu \delta \boldsymbol{\mu}^n \quad (26)$$

The stress, concentration, and flux are evaluated at integration points, depending on the gradients of the displacement and bio-chemical potential via the constitutive relations. Taking the gradient of Equation (26), we obtain that

$$\nabla_{\mathbf{x}} \delta \mathbf{u} = \nabla_{\mathbf{x}} \mathbf{H}^u \delta \mathbf{u}^n = \mathbf{B}^u \delta \mathbf{u}^n \quad (27a)$$

$$\tilde{\nabla}_{\tilde{\mathbf{x}}} \delta \mathbf{u} = \tilde{\nabla}_{\tilde{\mathbf{x}}} \mathbf{H}^u \delta \mathbf{u}^n = \tilde{\mathbf{B}}^u \delta \mathbf{u}^n \quad (27b)$$

$$\nabla_{\mathbf{x}} \delta \mu = \nabla_{\mathbf{x}} \mathbf{H}^\mu \delta \boldsymbol{\mu}^n = \mathbf{B}^\mu \delta \boldsymbol{\mu}^n \quad (27c)$$

$$\tilde{\nabla}_{\tilde{\mathbf{x}}} \delta \mu = \tilde{\nabla}_{\tilde{\mathbf{x}}} \mathbf{H}^\mu \delta \boldsymbol{\mu}^n = \tilde{\mathbf{B}}^\mu \delta \boldsymbol{\mu}^n \quad (27d)$$

where \mathbf{B}^u and \mathbf{B}^μ are the gradients of the shape functions in the bulk, and $\tilde{\mathbf{B}}^u$ and $\tilde{\mathbf{B}}^\mu$ are the ones on the surface.

4.4 Nonlinear solution

The weak form in Equation (24) can be expressed as a system of nonlinear equations,

$$\mathcal{N}(\mathbf{d}) = \mathbf{f} \quad \text{with} \quad \mathbf{d} = [\mathbf{u}^n \ \boldsymbol{\mu}^n]^T \quad (28)$$

We note that $\mathcal{N}(\mathbf{d})$ represents the unknown part of the weak form at the current time step. To obtain a solution, we move all the known quantities to the right-hand side and denote them as \mathbf{f} , which is given from the previous time step.

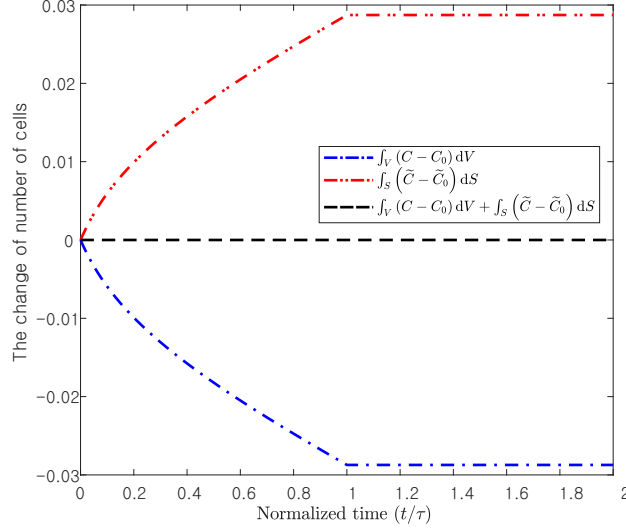


Figure 7: Contractile forces drive cells to move from the interior to the surface of the extracellular matrix (ECM). We track the number of species in both the bulk and on the surface over time. During the activation level ramping phase ($t/\tau < 1.0$), we observe an increase in the number of cells on surface and a decrease in bulk, while the total number of species remains constant. Once the activation level is fixed ($t/\tau \geq 1.0$), cell migration is suspended.

The residual of the nonlinear equations at iteration step i is then given by $\mathbf{R}_i = \mathbf{f} - \mathcal{N}(\mathbf{d}_i)$, which can be solved using the Newton-Raphson method. The method involves the calculation of the tangent Jacobian matrix at each iteration step, which is given by:

$$\left. \frac{\partial \mathcal{N}}{\partial \mathbf{d}} \right|_{\mathbf{d}_i} = \begin{bmatrix} \mathbf{K}^{\mathbf{u}\mathbf{u}} & \mathbf{K}^{\mathbf{u}\boldsymbol{\mu}} \\ \mathbf{K}^{\boldsymbol{\mu}\mathbf{u}} & \mathbf{K}^{\boldsymbol{\mu}\boldsymbol{\mu}} \end{bmatrix} \quad (29)$$

The coupled non-linear equations are numerically solved using FEniCS version 2019.2.0 [Logg et al., 2012, Alnæs et al., 2015], Multiphenics [Ballarin and Rozza, 2019] and the Portable Extensible Toolkit for Scientific Computations (PETSc) Scalable Nonlinear Equations Solvers (SNES) interface [Balay et al., 2019]. The solution process continues until a specified level of convergence is achieved within the SNES solver.

5 Results and discussion

To test the robustness of our numerical approach, and also the predictions corresponding to the specific model choices, we simulated two boundary value problems that we have studied experimentally in our previous work [Mailand et al., 2019, Sakar et al., 2016]. The first problem involves simulating the equilibrium morphology and cell distribution of microtissues during unperturbed morphogenesis in a microengineered *in vitro* platform. The second problem refers to simulating the equilibrium morphology and cell distribution of microtissues that are surgically perturbed using a robotic micromanipulation system. Figure 3 shows a schematic illustration of microtissues in their initial and final configurations for the two distinct cases. In the second case, a cylindrical hole is prescribed in the center of the reference state (see Figure 3b, left).

The boundary conditions for the two cases are identical, where the contact surfaces with the pillars are assumed to slide in the axial direction (z -direction) in a frictionless manner. The rest of the surface is considered to be traction-free, and rigid body motions are prevented. The initial normalized cell concentration is set to unity ($C/C_0 = \tilde{C}/\tilde{C}_0 = 1$) at the beginning of the simulation ($t/\tau = 0$), which determines the initial bio-chemical potentials ($\mu_0 = \tilde{\mu}_0 = 0$) through equations Equation (19e) and Equation (19f). The elastic modulus and Poisson's ratio are taken as $E = 17.38\text{kPa}$ and $\nu = 0.09$, respectively, resulting in bulk and shear moduli of $K = 7\text{kPa}$ and $G = 8\text{kPa}$ [Kim et al., 2020, 2023a]. The active moduli, $\alpha = 25\text{kPa}$, $\tilde{\alpha} = 2\text{mN/mm}$, $\beta = 50\text{kPa}$, and $\tilde{\beta} = 40\text{mN/mm}$, are calibrated using empirical characterization of the final tissue shape. The activation level of contractility is set to $n = 2$, and the time-normalized effective diffusivity was selected as $D\tau = \tilde{D}\tau = 1.0\text{m}^2\text{J}^{-1}$. The characteristic time is chosen as $\tau = 24\text{hr}$ based on observations that the tissues contracted at a significantly lower rate after the first 24 hours in previous experimental studies [Mailand et al., 2019, Kim et al., 2020]. The activation level of the cell contractility $\eta(t)$ drives the response in the simulations, while no external mechanical force is applied to the system. To maintain numerical stability, the

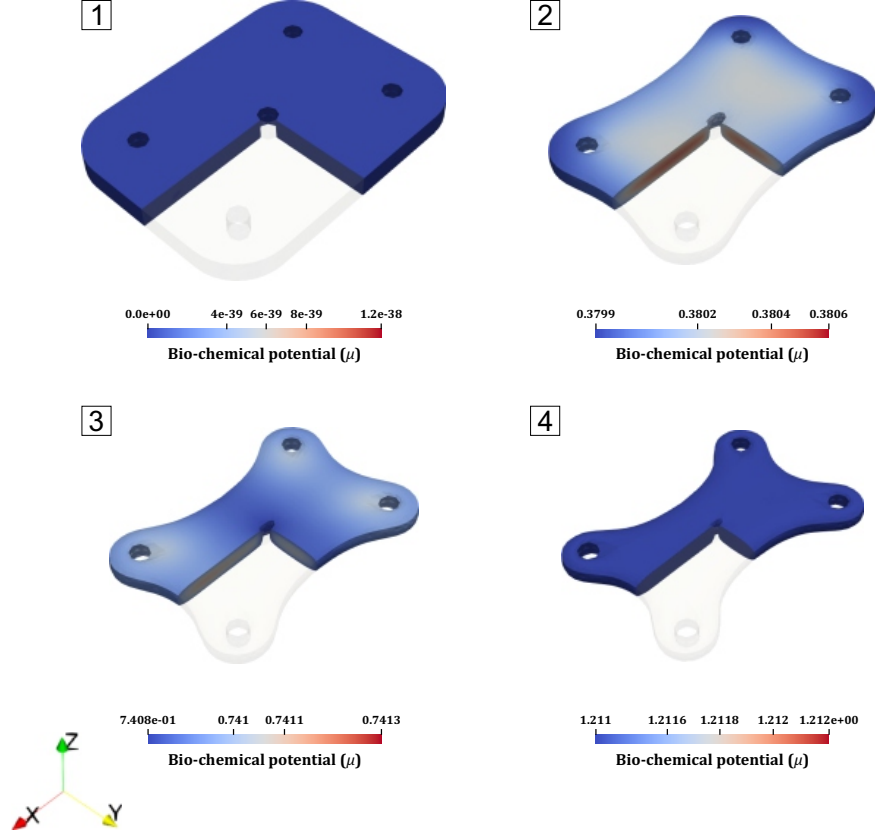


Figure 8: Temporal sequence of the bio-chemical potential during the formation of perturbed microtissues. A quarter of the domain is made transparent to show the contour plot on two sections of the interior.

activation level $\eta(t)$ is increased gradually from zero to its prescribed value for the time interval $t/\tau \in [0.0, 1.0]$, and then the time steps $\Delta t/\tau$ are exponentially increased until equilibrium is attained with the active moduli being fixed.

5.1 Time-dependent cell contractility and migration during tissue formation

In this section, we explore the nonlinear and transient response of microtissues during the uninterrupted morphogenesis process (see Figure 3a). We plot the temporal sequence of the finite element simulation for the bio-chemical potential, bulk concentration, and surface concentration in Figures 4 to 6, respectively, with images that are taken at normalized time $t/\tau = 0.0, 0.2, 0.5, 1.0$ (indicated by Step 1, 2, 3 and 4). In the initial stress-free undeformed state, corresponding to a cell-laden crosslinked hydrogel, the active free energies Ψ_a and $\tilde{\Psi}_a$ are taken as zero because we assume that the cells have not started interacting with the ECM yet (Step 1). Through the prescribed evolution law of $\eta(t)$ in Equation (17), the activation level is gradually increased from zero to unity as a function of time t , leading to microtissue contraction and cell migration. At low activation ($\eta = 0.2$), even at an early stage $t/\tau = 0.2$, the deformation is noticeable, and the mechanosensitive mechanisms captured by the proposed model guide the cells to the periphery of the microtissue and regions near the pillars (Step 2). Beyond $t/\tau = 0.5$, minimal migration and contractility are observed (Step 3). Finally, increased cell concentration near the periphery generates higher contraction, leading to smoother concave edges on the sides of the microtissue (Step 4).

In contrast to our previous theories [Kim et al., 2020, 2023a] where we assumed that the cell concentrations coincide in bulk and on the surface, i.e., $C|_S = \tilde{C}$, we can account for the distinct response here, as shown in Figures 5 and 6. On top of cell migration in bulk and on the surface, there is an exchange of cells between the surface and the bulk, as captured in the strong form of the balance law in Equation (8). Cell migration between bulk and surface can be tracked by integrating the normalized concentrations over the bulk and the surface at all time steps, where we observe cell migration from bulk to the surface while the total number of cells is conserved (Figure 7). To the best of the authors' knowledge, this is the first time such multiphysical biological processes have been studied in a macroscale simulation.

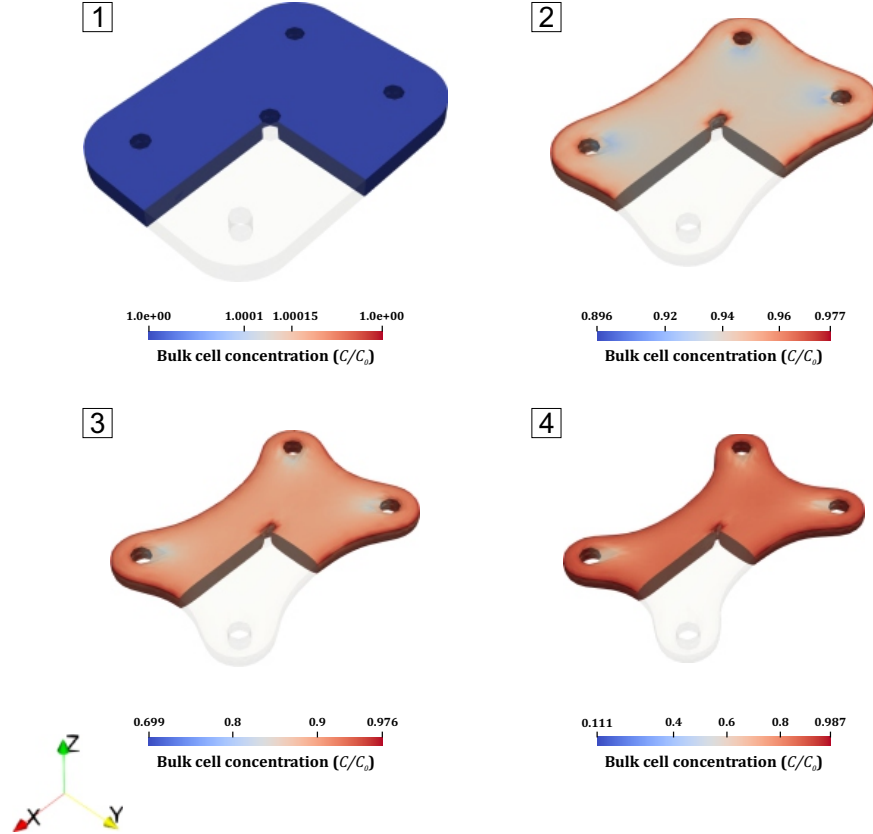


Figure 9: Temporal sequence of the bulk cell concentration during the formation of perturbed microtissues. A quarter of the domain is made transparent to show the contour plot on two sections of the interior.

5.2 Time-dependent cell contractility and migration during wound closure

In this section, we simulate a microtissue model with a hole in the center (see Figure 3b). All other dimensions, material properties, boundary conditions, as well as the ramping profile of activation are the same as in the previous example described in Section 5.1. The temporal sequence of the finite element simulations for the bio-chemical potential, bulk concentration, surface concentration are shown in Figures 8 to 10, respectively, with images that are taken at normalized time $t/\tau = 0.0, 0.2, 0.5, 1.0$ (indicated by Step 1, 2, 3 and 4). When the activation level is set to zero ($\eta = 0$), the perturbed microtissue is considered to be in a stress-free undeformed state with a hole in the center (Step 1). Through the prescribed evolution law of $\eta(t)$ in Equation (17), the activation level is gradually increased from zero to unity as a function of time t , leading to wound closure. At an early stage $t/\tau = 0.2$, the mechanosensitive mechanisms captured by the model guide the cells to the periphery of the wound hole and the outer boundary of microtissue (Step 2). Beyond $t/\tau = 0.5$, minimal migration and contractility are observed (Step 3). Finally, The cell migration and contractility result in effectively closing the wound hole, which we call the equilibrium state of perturbed microtissue (Step 4).

We further investigated the evolution of cell concentration of the perturbed microtissues to account for the distinct response of cells migration in bulk and on surface. We set the centerline at the middle of the bulk and on top of the surface, as shown in Figures 11a and 12a, respectively. The profiles of cell concentration along the centerlines are reported at the normalized time $t/\tau = 0.0, 0.25, 0.5, 0.75, 1.0$ with respect to the reference position. We can understand the local trend of cell migration by observing the decrease in bulk (Figure 11b) and the increase on surface (Figure 12b), which is consistent with the global trend of cell migration depicted in Figure 7. Furthermore, the results reveal the heterogeneous nature of cell migration along the centerline as the cell concentration at the boundaries of the microtissue and wound periphery are greater than those of the interior. The elevated cell concentration increases the surface energy, ultimately contributing to the closure of the wound. These results are consistent with the experimental observations reported in Sakar et al. [2016]. Fibroblasts move into the boundaries of the gap during the closure of the wound. Finally,

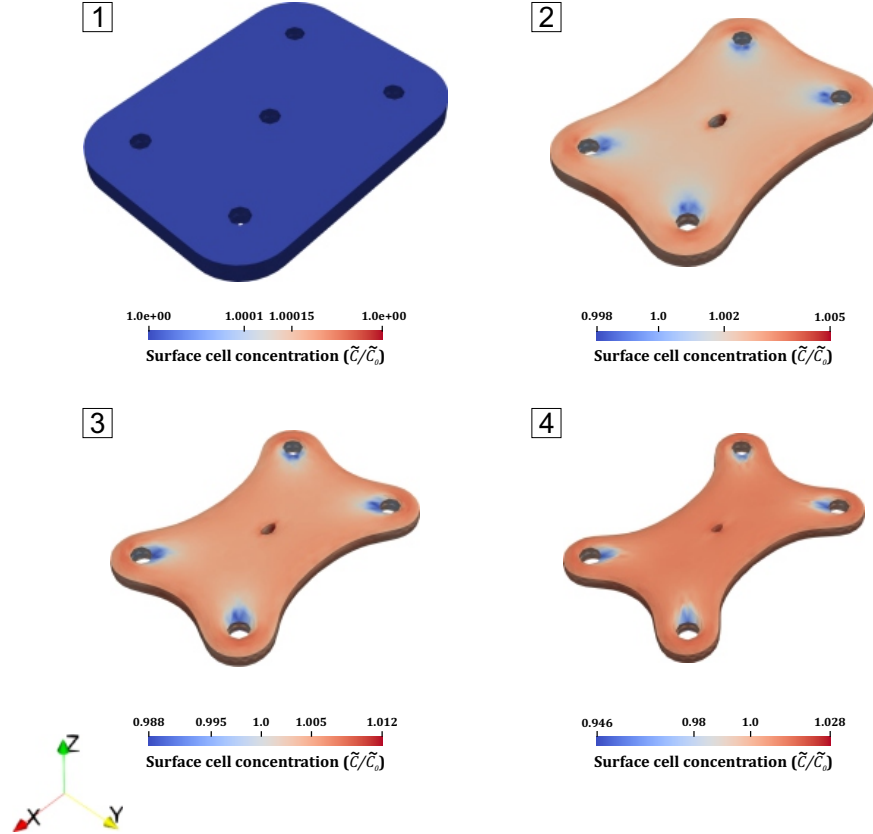


Figure 10: Temporal sequence of the surface cell concentration during the formation of perturbed microtissues.

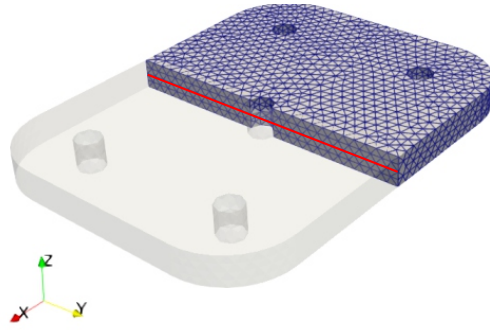
we plot the size of the wound hole in both the x and y directions over normalized time (Figure 13), and we observe a monotonic reduction in wound size, around $16 \mu\text{m}$, consistent with our experimental results [Sakar et al., 2016].

6 Conclusion

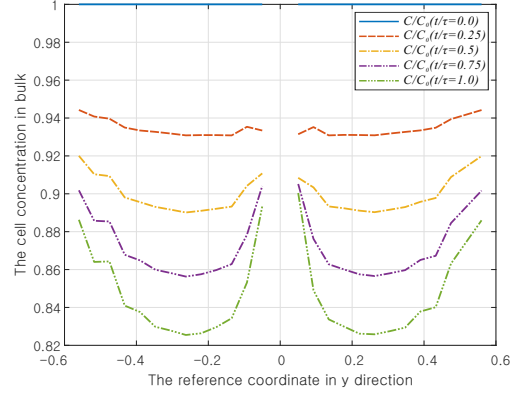
We introduce a continuum mechanics framework and corresponding open-source finite element implementation that considers the interaction between cellular contractility, migration, and ECM mechanics in dynamically morphing soft tissues. The proposed multiphysics model incorporates surface and bulk contractile stresses as well as surface and bulk cell kinetics driven by mechanosensing, and a direct coupling between the local deformation state and contractile force generation. Simulation results demonstrate the potential of our model to capture changes in tissue shape and cell concentration for both intact and mechanically manipulated microtissues. Such studies can provide valuable insights on cell-ECM interactions in the context of development, oncology, tissue engineering, and regenerative medicine.

This study reveals that cell migration in microtissues is influenced by the local geometry, with cells migrating towards the outer boundaries of the tissue and wound periphery. This directed migration is likely driven by the higher surface energy at the boundaries, which helps maintain the geometric integrity of the microtissues. During the early stages of morphogenesis, cells inside the microtissues exhibit high mobility and rapidly migrate towards the wound periphery. Notably, the migration pattern changes over time. In the early stage of cell migration ($t/\tau < 0.2$), we find that the initial cell migration is primarily determined by the geometry, as illustrated in Figures 5, 6, 9 and 10 Step 2. However, in late stages ($t/\tau > 0.5$), the geometry of the microtissue no longer has a significant effect, and the cell migration maintains the previous direction, as shown in Figures 5, 6, 9 and 10 Steps 3 and 4. In our future work, we will experimentally test these hypothesis by tracking cells using time-lapse imaging.

Taken together, our results suggest that local geometry is an important contributing factor that organizes cell migration in microtissues. From a computational standpoint, our approach is robust as we test multiple challenging and highly nonlinear boundary value problems with unique features. Interestingly, our implementation, which is based on a two-field weak form, overcomes numerical oscillation issues that arise near sharp features of the geometry in a three-field

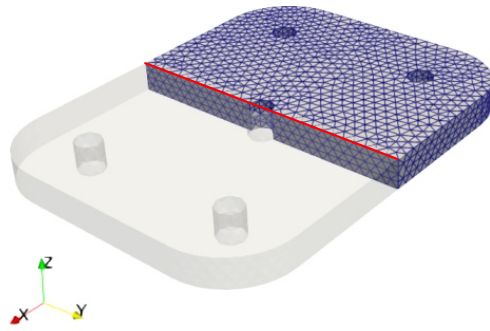


(a) The nodes on the red line are to be tracked over time.

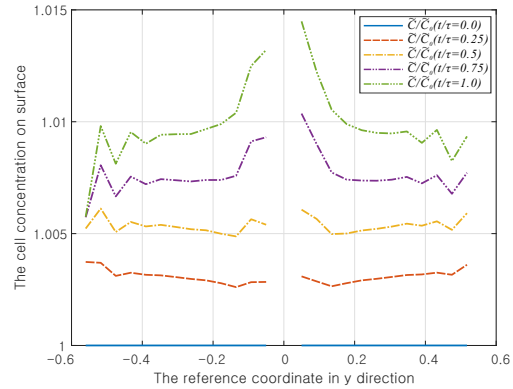


(b) The evolution of the bulk cell concentration on the red line.

Figure 11: During the activation level ramping phase, we obtain the bulk cell concentration of the perturbed microtissue along the centerline. We observe an overall decrease in bulk cell concentration, but there is an increase in concentration near the wound hole and microtissue boundaries as tissue formation progresses.



(a) The nodes on the red line are to be tracked over time.



(b) The evolution of the surface cell concentration on the red line.

Figure 12: During the activation level ramping phase, we obtain the surface cell concentration of the perturbed microtissue along the centerline. Our results show an overall increase in surface cell concentration, with a locally higher concentration near the wound hole.

weak form-based implementation for surface and bulk poroelasticity of hydrogels, as described in our previous work [Kim et al., 2023b].

Declaration of Competing Interest

The authors declare that they have no known competing financial interests or personal relationships that could have appeared to influence the work reported in this paper.

Acknowledgments

The authors thank prof. Berkin Dortdivanlioglu for pointing us to the work of Lucantonio et al. [2016].

A Thermodynamics considerations

Considering a system that includes an elastic collagen network coupled with cells that are free to migrate, its free energy, \mathcal{G} , has to account for these energetic contributions [Holzapfel, 2000, Gurtin et al., 2010, Hong et al., 2008, Bouklas

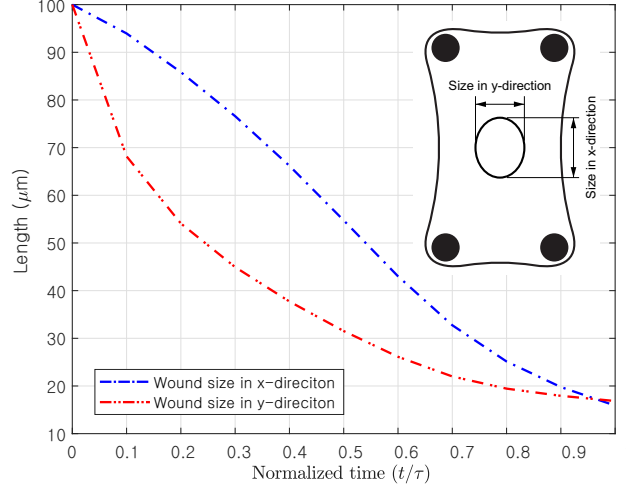


Figure 13: The proposed model successfully captures the wound closure process, as demonstrated by measuring the wound hole in two orthogonal directions. The results show that as the activation level ramps up, the wound gradually closes.

et al., 2015, Ang et al., 2020, Mao and Anand, 2018].

$$\dot{G} = \int_V \dot{\Psi} dV + \int_S \dot{\tilde{\Psi}} dS - \int_V \mathbf{B}\dot{\mathbf{x}} dV - \int_S \mathbf{T}\dot{\mathbf{x}} dS - \int_V \mu r dV - \int_S \tilde{\mu} i dS - \int_V \xi \dot{\eta} dV - \int_S \tilde{\xi} \dot{\tilde{\eta}} dS \quad (30)$$

where the third and fourth terms are the rate of mechanical work, which can be obtained by integrating Equation (7). The fifth and sixth terms are the rate of bio-chemical work, which can be obtained by integrating Equation (8). The seventh and eighth terms in the equation represent the microscopic force system, which is non-standard [Mao and Anand, 2018]. In this system, the microforces ξ and $\tilde{\xi}$ in the bulk and on the surface, respectively, are the energy conjugates of the rate of activation levels $\dot{\eta}$ and $\dot{\tilde{\eta}}$. Note that $\{\bullet\}$ is the time derivative of the quantity, and the thermodynamics dictate that the free energy of the system should not increase, i.e., $\dot{G} \leq 0$.

Consequently, coupling species diffusion and polymer deformation problem, the rate of change of the free energy of the system can be expressed as follows,

$$\begin{aligned} \dot{G} = & \int_V \dot{\Psi} dV + \int_S \dot{\tilde{\Psi}} dS - \int_V \mathbf{P} : \dot{\mathbf{F}} dV - \int_S \tilde{\mathbf{P}} : \dot{\tilde{\mathbf{F}}} dS - \int_V \mu \dot{C} dV - \int_S \tilde{\mu} \dot{\tilde{C}} dS \\ & - \int_V \xi \dot{\eta} dV - \int_S \tilde{\xi} \dot{\tilde{\eta}} dS + \int_S (\tilde{\mu} - \mu) \mathbf{J} \cdot \mathbf{N} dS + \int_V \mathbf{J} \cdot \nabla_{\mathbf{x}} \mu dV + \int_S \tilde{\mathbf{J}} \cdot \tilde{\nabla}_{\tilde{\mathbf{x}}} \tilde{\mu} dS \leq 0 \end{aligned} \quad (31)$$

Using the chain-rule, the rate of free energy densities can be written by

$$\dot{\Psi} = \frac{\partial \Psi}{\partial \mathbf{F}} : \dot{\mathbf{F}} + \frac{\partial \Psi}{\partial C} \dot{C} + \frac{\partial \Psi}{\partial \eta} \dot{\eta} \quad \text{and} \quad \dot{\tilde{\Psi}} = \frac{\partial \tilde{\Psi}}{\partial \tilde{\mathbf{F}}} : \dot{\tilde{\mathbf{F}}} + \frac{\partial \tilde{\Psi}}{\partial \tilde{C}} \dot{\tilde{C}} + \frac{\partial \tilde{\Psi}}{\partial \tilde{\eta}} \dot{\tilde{\eta}} \quad (32)$$

By substituting Equation (32) into Equation (31), and rearranging terms yields

$$\begin{aligned} \dot{G} = & \int_V \left(\frac{\partial \Psi}{\partial \mathbf{F}} - \mathbf{P} \right) : \dot{\mathbf{F}} dV + \int_S \left(\frac{\partial \tilde{\Psi}}{\partial \tilde{\mathbf{F}}} - \tilde{\mathbf{P}} \right) : \dot{\tilde{\mathbf{F}}} dS + \int_V \left(\frac{\partial \Psi}{\partial C} - \mu \right) \dot{C} dV + \int_S \left(\frac{\partial \tilde{\Psi}}{\partial \tilde{C}} - \tilde{\mu} \right) \dot{\tilde{C}} dS \\ & + \int_V \left(\frac{\partial \Psi}{\partial \eta} - \xi \right) \dot{\eta} dV + \int_S \left(\frac{\partial \tilde{\Psi}}{\partial \tilde{\eta}} - \tilde{\xi} \right) \dot{\tilde{\eta}} dS + \int_S (\tilde{\mu} - \mu) \mathbf{J} \cdot \mathbf{N} dS + \int_V \mathbf{J} \cdot \nabla_{\mathbf{x}} \mu dV + \int_S \tilde{\mathbf{J}} \cdot \tilde{\nabla}_{\tilde{\mathbf{x}}} \tilde{\mu} dS \leq 0 \end{aligned} \quad (33)$$

where each integral represents a distinct mechanism of energy dissipation, associated with mechanical and bio-chemical, and microscopic works. The inequality must hold at every point of the continuum body and for all times during a thermodynamic process. Therefore, every individual integrand in Equation (33) must either be negative or vanish.

References

- Silvia S Chen, Wendy Fitzgerald, Joshua Zimmerberg, Hynda K Kleinman, and Leonid Margolis. Cell-cell and cell-extracellular matrix interactions regulate embryonic stem cell differentiation. *Stem cells*, 25(3):553–561, 2007.
- Wu Ma, Tara Tavakoli, Eric Derby, Yevgeniya Serebryakova, Mahendra S Rao, and Mark P Mattson. Cell-extracellular matrix interactions regulate neural differentiation of human embryonic stem cells. *BMC developmental biology*, 8(1): 1–13, 2008.
- Fiona M Watt and Hironobu Fujiwara. Cell-extracellular matrix interactions in normal and diseased skin. *Cold Spring Harbor Perspectives in Biology*, 3(4):a005124, 2011.
- Christine E Schmidt and Jennie M Baier. Acellular vascular tissues: natural biomaterials for tissue repair and tissue engineering. *Biomaterials*, 21(22):2215–2231, 2000.
- Adrián Buganza Tepole. Computational systems mechanobiology of wound healing. *Computer methods in applied mechanics and engineering*, 314:46–70, 2017.
- RA Brown, R Prajapati, DA McGrouther, IV Yannas, and M Eastwood. Tensional homeostasis in dermal fibroblasts: Mechanical responses to mechanical loading in three-dimensional substrates. *Journal of cellular physiology*, 175(3): 323–332, 1998.
- Jay D Humphrey. Continuum biomechanics of soft biological tissues. *Proceedings of the Royal Society of London. Series A: Mathematical, Physical and Engineering Sciences*, 459(2029):3–46, 2003.
- Jonas F Eichinger, Lea J Haeusel, Daniel Paukner, Roland C Aydin, Jay D Humphrey, and Christian J Cyron. Mechanical homeostasis in tissue equivalents: a review. *Biomechanics and modeling in mechanobiology*, pages 1–18, 2021a.
- Boris Hinz, Sem H Phan, Victor J Thannickal, Marco Prunotto, Alexis Desmoulière, John Varga, Olivier De Wever, Marc Mareel, and Giulio Gabbiani. Recent developments in myofibroblast biology: paradigms for connective tissue remodeling. *The American journal of pathology*, 180(4):1340–1355, 2012.
- Shirin Nour, Nafiseh Baheiraee, Rana Imani, Mohammad Khodaei, Akram Alizadeh, Navid Rabiee, and S Mohammad Moazzeni. A review of accelerated wound healing approaches: biomaterial-assisted tissue remodeling. *Journal of Materials Science: Materials in Medicine*, 30:1–15, 2019.
- Anna Q Cai, Kerry A Landman, and Barry D Hughes. Multi-scale modeling of a wound-healing cell migration assay. *Journal of Theoretical Biology*, 245(3):576–594, 2007.
- Frederick Grinnell and W Matthew Petroll. Cell motility and mechanics in three-dimensional collagen matrices. *Annual review of cell and developmental biology*, 26:335–361, 2010.
- Tadanori Mammoto and Donald E Ingber. Mechanical control of tissue and organ development. *Development*, 137(9): 1407–1420, 2010.
- Jasper Foolen, Tadahiro Yamashita, and Philip Kollmannsberger. Shaping tissues by balancing active forces and geometric constraints. *Journal of Physics D: Applied Physics*, 49(5):053001, 2015.
- Catarina Leite Pereira, Graciosa Q Teixeira, Cláudia Ribeiro-Machado, Joana Caldeira, Madalena Costa, Francisco Figueiredo, Rui Fernandes, Paulo Aguiar, Sibylle Grad, Mário A Barbosa, et al. Mesenchymal stem/stromal cells seeded on cartilaginous endplates promote intervertebral disc regeneration through extracellular matrix remodeling. *Scientific Reports*, 6(1):1–17, 2016.
- Sjoerd Van Helvert, Cornelis Storm, and Peter Friedl. Mechanoreciprocity in cell migration. *Nature cell biology*, 20(1): 8, 2018.
- Maja Matis. The mechanical role of microtubules in tissue remodeling. *BioEssays*, 42(5):1900244, 2020.
- Eugene Bell, Bengt Ivarsson, and Charlotte Merrill. Production of a tissue-like structure by contraction of collagen lattices by human fibroblasts of different proliferative potential in vitro. *Proceedings of the National Academy of Sciences*, 76(3):1274–1278, 1979.
- David Stopak and Albert K Harris. Connective tissue morphogenesis by fibroblast traction: I. tissue culture observations. *Developmental biology*, 90(2):383–398, 1982.
- Andrew W Holle, Jennifer L Young, and Joachim P Spatz. In vitro cancer cell–ecm interactions inform in vivo cancer treatment. *Advanced drug delivery reviews*, 97:270–279, 2016.
- Jonas F Eichinger, Maximilian J Grill, Iman Davoodi Kermani, Roland C Aydin, Wolfgang A Wall, Jay D Humphrey, and Christian J Cyron. A computational framework for modeling cell-matrix interactions in soft biological tissues. *arXiv preprint arXiv:2103.13110*, 2021b.
- Jaemin Kim, Erik Mailand, Mahmut Selman Sakar, and Nikolaos Bouklas. A model for mechanosensitive cell migration in dynamically morphing soft tissues. *Extreme Mechanics Letters*, 58:101926, 2023a.

- M Reza Shaebani, Adam Wysocki, Roland G Winkler, Gerhard Gompper, and Heiko Rieger. Computational models for active matter. *Nature Reviews Physics*, pages 1–19, 2020.
- Haiqin Wang and Xinpeng Xu. Continuum elastic models for force transmission in biopolymer gels. *Soft Matter*, 16(48):10781–10808, 2020.
- Helen Byrne and Dirk Drasdo. Individual-based and continuum models of growing cell populations: a comparison. *Journal of mathematical biology*, 58(4):657–687, 2009.
- Wesley R Legant, Amit Pathak, Michael T Yang, Vikram S Deshpande, Robert M McMeeking, and Christopher S Chen. Microfabricated tissue gauges to measure and manipulate forces from 3d microtissues. *Proceedings of the National Academy of Sciences*, 106(25):10097–10102, 2009.
- Vikram S Deshpande, Robert M McMeeking, and Anthony G Evans. A bio-chemo-mechanical model for cell contractility. *Proceedings of the National Academy of Sciences*, 103(38):14015–14020, 2006.
- Franck J Vernerey and Mehdi Farsad. A constrained mixture approach to mechano-sensing and force generation in contractile cells. *Journal of the mechanical behavior of biomedical materials*, 4(8):1683–1699, 2011.
- Vivek B Shenoy, Hailong Wang, and Xiao Wang. A chemo-mechanical free-energy-based approach to model durotaxis and extracellular stiffness-dependent contraction and polarization of cells. *Interface focus*, 6(1):20150067, 2016.
- Ehsan Ban, J Matthew Franklin, Sungmin Nam, Lucas R Smith, Hailong Wang, Rebecca G Wells, Ovijit Chaudhuri, Jan T Liphardt, and Vivek B Shenoy. Mechanisms of plastic deformation in collagen networks induced by cellular forces. *Biophysical journal*, 114(2):450–461, 2018.
- Ismael González-Valverde and José Manuel García-Aznar. Mechanical modeling of collective cell migration: An agent-based and continuum material approach. *Computer Methods in Applied Mechanics and Engineering*, 337:246–262, 2018.
- Brendon M Baker, Britta Trappmann, William Y Wang, Mahmut S Sakar, Iris L Kim, Vivek B Shenoy, Jason A Burdick, and Christopher S Chen. Cell-mediated fibre recruitment drives extracellular matrix mechanosensing in engineered fibrillar microenvironments. *Nature materials*, 14(12):1262–1268, 2015.
- AS Abhilash, Brendon M Baker, Britta Trappmann, Christopher S Chen, and Vivek B Shenoy. Remodeling of fibrous extracellular matrices by contractile cells: predictions from discrete fiber network simulations. *Biophysical journal*, 107(8):1829–1840, 2014.
- Shiladitya Banerjee and M Cristina Marchetti. Continuum models of collective cell migration. *Cell Migrations: Causes and Functions*, pages 45–66, 2019.
- Jaemin Kim, Erik Mailand, Ida Ang, Mahmut Selman Sakar, and Nikolaos Bouklas. A model for 3d deformation and reconstruction of contractile microtissues. *Soft Matter*, 2020.
- Erik Mailand, Ece Özelçi, Jaemin Kim, Matthias Rüegg, Odysseas Chaliotis, Jon Märki, Nikolaos Bouklas, and Mahmut Selman Sakar. Tissue engineering with mechanically induced solid-fluid transitions. *Advanced Materials*, page 2106149, 2021.
- Wesley R Legant, Christopher S Chen, and Viola Vogel. Force-induced fibronectin assembly and matrix remodeling in a 3d microtissue model of tissue morphogenesis. *Integrative Biology*, 4(10):1164–1174, 2012.
- Raimon Sunyer, Vito Conte, Jorge Escribano, Alberto Elosegui-Artola, Anna Labernadie, Léo Valon, Daniel Navajas, José Manuel García-Aznar, José J Muñoz, Pere Roca-Cusachs, et al. Collective cell durotaxis emerges from long-range intercellular force transmission. *Science*, 353(6304):1157–1161, 2016.
- Joshua M Grolman, Philipp Weinand, and David J Mooney. Extracellular matrix plasticity as a driver of cell spreading. *Proceedings of the National Academy of Sciences*, 117(42):25999–26007, 2020.
- Erik Mailand, Bin Li, Jeroen Eyckmans, Nikolaos Bouklas, and Mahmut Selman Sakar. Surface and bulk stresses drive morphological changes in fibrous microtissues. *Biophysical journal*, 117(5):975–986, 2019.
- AT McBride, A Javili, P Steinmann, and Swantje Bargmann. Geometrically nonlinear continuum thermomechanics with surface energies coupled to diffusion. *Journal of the Mechanics and Physics of Solids*, 59(10):2116–2133, 2011.
- Alessandro Lucantonio, Luciano Teresi, and Antonio DeSimone. Continuum theory of swelling material surfaces with applications to thermo-responsive gel membranes and surface mass transport. *Journal of the Mechanics and Physics of Solids*, 89:96–109, 2016.
- Jaemin Kim, Ida Ang, Francesco Ballarin, Chung-Yuen Hui, and Nikolaos Bouklas. A finite element implementation of finite deformation surface and bulk poroelasticity. *arXiv preprint arXiv:2305.08805*, 2023b.
- Gerhard A Holzapfel. *Nonlinear solid mechanics II*. John Wiley & Sons, Inc., 2000.

- Paul Steinmann. On boundary potential energies in deformational and configurational mechanics. *Journal of the Mechanics and Physics of Solids*, 56(3):772–800, 2008.
- Albert Edward Green and Wolfgang Zerna. *Theoretical elasticity*. Courier Corporation, 1992.
- Manfredo P Do Carmo. *Differential geometry of curves and surfaces: revised and updated second edition*. Courier Dover Publications, 2016.
- Morton E Gurtin, Eliot Fried, and Lallit Anand. *The mechanics and thermodynamics of continua*. Cambridge University Press, 2010.
- Nikolaos Bouklas and Rui Huang. Swelling kinetics of polymer gels: comparison of linear and nonlinear theories. *Soft Matter*, 8(31):8194–8203, 2012.
- Jay D Humphrey, Eric R Dufresne, and Martin A Schwartz. Mechanotransduction and extracellular matrix homeostasis. *Nature reviews Molecular cell biology*, 15(12):802–812, 2014.
- W Matthew Petroll, Mridula Vishwanath, and Lisha Ma. Corneal fibroblasts respond rapidly to changes in local mechanical stress. *Investigative ophthalmology & visual science*, 45(10):3466–3474, 2004.
- Matthew J Paszek, Nastaran Zahir, Kandice R Johnson, Johnathon N Lakins, Gabriela I Rozenberg, Amit Gefen, Cynthia A Reinhart-King, Susan S Margulies, Micah Dembo, David Boettiger, et al. Tensional homeostasis and the malignant phenotype. *Cancer cell*, 8(3):241–254, 2005.
- Andrew D Doyle, Francis W Wang, Kazue Matsumoto, and Kenneth M Yamada. One-dimensional topography underlies three-dimensional fibrillar cell migration. *Journal of cell biology*, 184(4):481–490, 2009.
- Pierre Delvoye, Philippe Wiliquet, Jean-Luc Levêque, Betty V Nusgens, and Charles M Lapière. Measurement of mechanical forces generated by skin fibroblasts embedded in a three-dimensional collagen gel. *Journal of Investigative Dermatology*, 97(5):898–902, 1991.
- Mark Eastwood, Rebecca Porter, Umraz Khan, Gus McGrouther, and Robert Brown. Quantitative analysis of collagen gel contractile forces generated by dermal fibroblasts and the relationship to cell morphology. *Journal of cellular physiology*, 166(1):33–42, 1996.
- Jonas F Eichinger, Daniel Paukner, Jason M Szafron, Roland C Aydin, Jay Dowell Humphrey, and Christian J Cyron. Computer-controlled biaxial bioreactor for investigating cell-mediated homeostasis in tissue equivalents. *Journal of biomechanical engineering*, 142(7), 2020.
- Nikolaos Bouklas, Chad M Landis, and Rui Huang. A nonlinear, transient finite element method for coupled solvent diffusion and large deformation of hydrogels. *Journal of the Mechanics and Physics of Solids*, 79:21–43, 2015.
- Wei Hong, Xuanhe Zhao, Jinxiong Zhou, and Zhigang Suo. A theory of coupled diffusion and large deformation in polymeric gels. *Journal of the Mechanics and Physics of Solids*, 56(5):1779–1793, 2008.
- Douglas N Arnold, Franco Brezzi, and Michel Fortin. A stable finite element for the stokes equations. *Calcolo*, 21(4):337–344, 1984.
- Daniele Boffi, Franco Brezzi, Michel Fortin, et al. *Mixed finite element methods and applications*, volume 44. Springer, 2013.
- Anders Logg, Kent-Andre Mardal, Garth N. Wells, et al. *Automated Solution of Differential Equations by the Finite Element Method*. Springer, 2012. ISBN 978-3-642-23098-1. doi:10.1007/978-3-642-23099-8.
- Martin S. Alnæs, Jan Blechta, Johan Hake, August Johansson, Benjamin Kehlet, Anders Logg, Chris Richardson, Johannes Ring, Marie E. Rognes, and Garth N. Wells. The fenics project version 1.5. *Archive of Numerical Software*, 3(100), 2015. doi:10.11588/ans.2015.100.20553.
- F Ballarin and G Rozza. multiphenics-easy prototyping of multiphysics problems in fenics. URL <https://mathlab.sissa.it/multiphenics>, 2019.
- Satish Balay, Shrirang Abhyankar, Mark Adams, Jed Brown, Peter Brune, Kris Buschelman, Lisandro Dalcin, Alp Dener, Victor Eijkhout, W Gropp, et al. *Petsc users manual*. 2019.
- Mahmut Selman Sakar, Jeroen Eyckmans, Roel Pieters, Daniel Eberli, Bradley J Nelson, and Christopher S Chen. Cellular forces and matrix assembly coordinate fibrous tissue repair. *Nature communications*, 7(1):1–8, 2016.
- Ida Ang, Zezhou Liu, Jaemin Kim, Chung-Yuen Hui, and Nikolaos Bouklas. Effect of elastocapillarity on the swelling kinetics of hydrogels. *Journal of the Mechanics and Physics of Solids*, page 104132, 2020.
- Yunwei Mao and Lallit Anand. A theory for fracture of polymeric gels. *Journal of the Mechanics and Physics of Solids*, 115:30–53, 2018.